Available online at www.sciencedirect.com
SCIENCE DIRECT®
Precision Engineering 30 (2006) 306–313
PRECISION ENGINEERING
www.elsevier.com/locate/precision

Bench-top setup for validation of real time, digital periodic error correction

Tony L. Schmitz [a,*], Lonnie Houck III [a], David Chu [b], Lee Kalem [b]

[a] *University of Florida, 237 MAE-B, Gainesville, FL 32611, Unites States*
[b] *Agilent Technologies Inc., P.O. Box 58059, Santa Clara, CA 95052, United States*

Received 11 May 2005; accepted 31 October 2005
Available online 6 January 2006

Abstract

This paper provides experimental validation of the digital first-order periodic error reduction scheme described by Chu and Ray. A bench-top setup of a single-pass, heterodyne Michelson interferometer, designed to minimize common error contributors such as Abbe, dead path and environment, is described. Linear, reciprocating motion generation is achieved using a parallelogram, leaf-type flexure. Periodic error amplitude is varied through independent rotation of a half wave plate and polarizer. Experimental results demonstrate that the correction algorithm can successfully attenuate first-order error to sub-nm levels for a wide range of frequency mixing conditions.

Keywords: Interferometry; Heterodyne; Displacement; Nonlinearity; Cyclic

1. Introduction

Differential-path interferometry is used extensively in situations requiring accurate displacement measurements. Examples include lithographic stages for semiconductor fabrication, transducer calibration and axis position feedback for precision cutting and measuring machines. In many applications, a dual frequency (heterodyne) Michelson-type interferometer with single, double or multiple passes of the optical paths is implemented. These systems infer changes in displacement of a selected optical path by monitoring the optically induced variation in a photodetector current. The phase-measuring electronics convert this photodetector current to displacement by digitizing the phase progression of the photodetector signal. Due to non-ideal performance, mixing between the two heterodyne frequencies may occur, which results in periodic errors superimposed on the desired displacement data (i.e., the error amplitude varies cyclically with the target position). In practice, first-order periodic error, which appears as single sideband modulation on the data at a spatial frequency of one cycle per displacement fringe, often dominates. Second-order periodic error, with a spatial frequency of two cycles per displacement fringe, is also commonly observed.

Although modifications to traditional optical setups may be implemented to reduce periodic error, it is often inconvenient to make changes to existing configurations. Additionally, the extra optical components and/or hardware generally necessary to achieve decreased periodic error can be costly. As an alternative to changes in the interferometer setup, Chu and Ray have recently described a scheme to correct first-order periodic error in real time using digital logic hardware [1]. An overview is provided in Section 3.

The purpose of this study is to validate of the Chu and Ray approach using a bench-top setup of a single-pass, heterodyne Michelson-type interferometer. The setup enables: (1) isolation of periodic error as the primary uncertainty source in displacement measuring interferometry; (2) variation of the frequency mixing that leads to periodic error so that the error amplitude may be changed. During target motion, the real time first-order error correction is digitally applied in hardware and both the corrected and uncorrected measurement signals are recorded. Various frequency mixing levels are realized by adjustment of the setup optics; the periodic error levels before and after correction are presented for multiple cases.

2. Background

In this work we focus on heterodyne Michelson-type interferometers. In these systems, imperfect separation of the two

* Corresponding author. Tel.: +1 352 392 8909; fax: +1 352 392 1071.
E-mail address: tschmitz@ufl.edu (T.L. Schmitz).

0141-6359/$ – see front matter © 2005 Elsevier Inc. All rights reserved.
doi:10.1016/j.precisioneng.2005.10.001

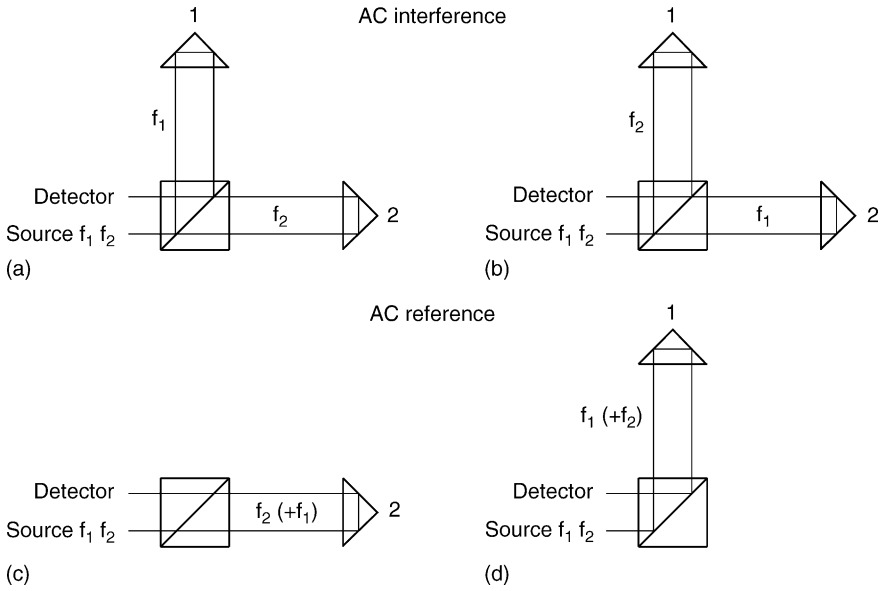

Fig. 1. Physical sources of *ac interference* and *ac reference* terms: (a) the intended *ac interference* term is derived from interference of frequency 1, f_1, light following path 1 and f_2 light following path 2; (b) the leakage-induced *ac interference* term, which occurs when the f_1 light follows path 2 and vice versa, causes second-order error; (c) and (d) *ac reference* terms are generated when both frequencies exist in a single path and lead to first-order periodic error [33].

light frequencies into the measurement (moving) and reference (fixed) paths has been shown to produce first- and second-order periodic errors. The two heterodyne frequencies are typically carried on collinear, mutually orthogonal, linearly polarized laser beams in a method referred to as polarization-coding. Unwanted leakage of the reference frequency into the measurement path, and vice versa, may occur due to non-orthogonality between the ideally linear beam polarizations, elliptical polarization of the individual beams, imperfect optical components, parasitic reflections from individual optical surfaces and/or mechanical misalignment between the interferometer elements (laser, polarizing optics and targets). In a perfect system, a single frequency would travel to a fixed target, while a second, single frequency traveled to a moving target. Interference of the combined signals would yield a perfectly sinusoidal trace with phase that varied, relative to a reference phase signal, in response to motion of the moving target. However, the inherent frequency leakage in actual implementations produces an interference signal, which is not purely sinusoidal (i.e., contains spurious spectral content) and leads to periodic error in the measured displacement.

Fedotova [2], Quenelle [3], and Sutton [4] performed early investigations of periodic error in heterodyne Michelson interferometers. Subsequent publications identified and described these periodic errors and built on the previous work [5–32]. Specific areas of research have included efforts to measure periodic error under various conditions (e.g., references [5–8]), frequency domain analyses [9–11], analytical modeling techniques [12–16], Jones calculus modeling methods [8,17] and reduction of periodic errors (e.g., references [9,18,30,32]).

Schmitz and Beckwith [33] summarize the potential periodic error contributors using a frequency–path, or F–P, model, which identifies each possible path for each light frequency from the source to detector and predicts the number of interference terms that may be expected at the detector output. For the single-pass, heterodyne Michelson interferometer used in this study, it is shown that 10 distinct interference terms exist in a fully leaking interferometer (i.e., both frequencies exist in both the measurement and reference paths). However, these interference terms may be grouped by optical path change dependency into only four categories: (1) o*ptical power* which contributes a constant intensity to the photodetector current independent of optical path changes; (2) *ac reference* terms with phase that varies by one full cycle over the synthetic wavelength, or the distance defined by the difference in wave numbers (i.e., the reciprocal of the wavelength) between the source frequencies in question and occur at the split frequency, or the difference between the heterodyne frequencies; (3) *dc interference*, which are Doppler shifted up from zero frequency during target motion and represent the signal of choice in homodyne interferometers; (4) *dc interference* terms which produce a time harmonic variation in the detector current at the split frequency and are Doppler shifted up or down during target motion depending on direction. With respect to periodic errors, the leakage-induced *ac interference* term leads to second-order error, while the *ac reference* terms cause first-order error. The physical sources of the *ac interference* and *ac reference* terms are shown in Fig. 1.

3. Overview of error correction approach

3.1. Periodic error measurement

In Chu and Ray's method [1], first-order periodic error, Δs, is modeled as a periodic function of ideal position s as $\Delta\phi = \frac{1}{2\pi}\tan^{-1}\left[\frac{r\sin(-2\pi(\phi-\theta))}{1+r\cos(-2\pi(\phi-\theta))}\right]$, where $\Delta\phi = \frac{2\Delta s}{\lambda}$ and $\phi = \frac{2s}{\lambda}$ are expressed in unit intervals, UI, where $1\,\text{UI} = 2\pi$ rad. This represents a single sideband (SSB) modu-

lation of a unity magnitude main signal by a perturbing signal of fractional size r, which generates a spatially coherent disturbance of one cycle per fringe at a phase shift θ. Both quasi-static parameters r and θ are measured by a 'best fit' regression process performed on ~1 ms of uncorrected data (320 points at a sampling frequency of 312.5 kHz). These are immediately used to correct the following 1 ms of data. The measure-correct process continues in a leapfrog manner so that all but the first latent 1 ms of data are corrected in real time. The reader may note that this r perturbation form is equivalent to the *ac reference* terms described in Section 2 (and identified in Fig. 1), which occur at the heterodyne interferometer split frequency and sum vectorally with the intended, Doppler shifted *ac interference* term.

In measurement (but not in correction), the periodic error is modeled as a pure sinusoid. The sum of a parabola and sinusoid are 'best fit' to a sequence of 320 position data points, expressed in UI. Macroscopic motion up to constant acceleration is removed. Therefore, excessive jerk (or the time derivative of acceleration) reduces the effectiveness of this approach. The mathematical model is expressed as:

$$\phi_j \approx x_0 + x_1 \cdot j + x_2 \cdot k + x_c \cdot \cos(2\pi\phi_j) + x_s \cdot \sin(2\pi\phi_j). \tag{1}$$

A column of '1's forms a unity vector, **I**. Index j steps by 1 from −159.5 to +159.5 to form a linear vector, **J**. Index k spans from −16395 to 16395, stepping by $2j+1$, to form a quadratic vector, **K**. Columns of $\cos(2\pi\phi_j)$ and $\sin(2\pi\phi_j)$ form the cosine vector **C** and the sine vector **S**, respectively. The five columns vectors **I**, **J**, **K**, **C** and **S** are combined to form a 320×5 matrix, **M**. These 320 equations, written in matrix form, become $\mathbf{MX} = \mathbf{P}$, where **P** is the column of uncorrected position data and the column of five unknowns, x_i, contained in the vector, **X**, are determined from the traditional min-squared regression solution $\mathbf{X} = (\mathbf{M^T M})^{-1}\mathbf{M^T P}$. This implies that the most effective regression operator is $\mathbf{M^T}$. Computation is immensely simplified, however, if a simpler operator $\mathbf{O^T}$ with a restricted alphabet (1, 0, −1 and −2) is chosen to mimic $\mathbf{M^T}$. The best fit solution then becomes:

$$\mathbf{X} = (\mathbf{O^T M})^{-1}\mathbf{O^T P}. \tag{2}$$

Simple elements enable matrix multiplications $\mathbf{O^T M}$ and $\mathbf{O^T P}$ to be synthesized using ordinary high-speed digital accumulators. The five columns of **O** are named **U**, **L**, **Q**, **E**, and **D**. They are selected so that $\mathbf{U^T I} = 2^8$, $\mathbf{L^T J} = 2^{14}$, $\mathbf{Q^T K} = 2^{21}$, and $\mathbf{U^T J} = \mathbf{U^T K} = \mathbf{L^T I} = \mathbf{L^T K} = \mathbf{Q^T I} = \mathbf{Q^T J} = 0$. Matrix inversion $(\mathbf{O^T M})^{-1}$ is greatly simplified (and accelerated) by vector orthogonality and diagonal powers of 2.

For 'block regression', the columns of **O** are arranged in 10 blocks of 32 identical elements expressed as: $\mathbf{U^T} = (1, 1, 0, 1, 1, 1, 1, 0, 1, 1)$; $\mathbf{L^T} = (-1, -1, 0, 0, 0, 0, 0, 0, 1, 1)$; $\mathbf{Q^T} = (1, 1, 0, 0, -2, -2, 0, 0, 1, 1)$; $\mathbf{E^T} = (e, e, e, e, e, e, e, e, e, e)$; $\mathbf{D^T} = (d, d, d, d, d, d, d, d, d, d)$. For example, the first element, 1, in $\mathbf{U^T}$ is repeated 32 times, the second element, 1, is repeated 32 times and so on to give a total vector length of 320. The elements e and d in $\mathbf{E^T}$ and $\mathbf{D^T}$, respectively, are quantized versions of the cosine and sine functions, equaling 1 whenever the function exceeds 0.707, −1 when less than −0.707, and 0 otherwise. The periodic error magnitude V, equal to $r/(2\pi)$, and phase θ are derived from two of the five unknowns in the **X** vector, i.e., $V = \sqrt{x_c^2 + x_s^2}$ and $\theta = \left(\frac{1}{2\pi}\right)\tan^{-1}\left(\frac{x_c}{-x_s}\right)$, where the quadrant dependence of the tangent function must be observed in implementation. These parameters, in UI form, are used to correct periodic error in the next batch of data.

3.2. Periodic error correction

The SSB nature of the perturbation is taken into consideration during correction. By approximation, the periodic error in UI, $\Delta\phi = \frac{2\,\Delta s}{\lambda}$, can be rewritten, as:

$$\Delta\phi(\phi) = \left(\frac{1}{2\pi}\right)\tan^{-1}\left[\frac{r\,\sin(-2\pi(\phi-\theta))}{1 + r\,\cos(-2\pi(\phi-\theta))}\right] \tag{3}$$

$$\Delta\phi(\phi) \approx \frac{(r/2\pi)\sin(-2\pi(\phi-\theta))}{1 + 2\pi(r/2\pi)\cos(-2\pi(\phi-\theta))} = \frac{V\,\sin(-2\pi(\phi-\theta))}{1 + 2V\pi\,\cos(-2\pi(\phi-\theta))}$$

$$\Delta\phi(\phi) \approx -V\,\sin(-2\pi(\phi-\theta)) + V^2\pi\,\sin(-4\pi(\phi-\theta))$$

For correction convenience, the periodic error $\Delta\phi$ should be expressed as a function of the readily available uncorrected position ϕ_j, rather than the ideal position ϕ. From calculus, $\Delta\phi(x - \Delta x) \approx \Delta\phi(x) - \Delta'\phi(x)\cdot\Delta x$. Substituting ϕ_j for x and $(\phi_j - \phi)$ for Δx, the calculus equation becomes $(\phi_j - \phi) \equiv \Delta\phi(\phi) \approx \Delta\phi(\phi_j) - \Delta'\phi(\phi_j)\cdot(\phi_j - \phi)$. Solving for $(\phi_j - \phi) = \frac{\Delta\phi(\phi_j)}{1+\Delta'\phi(\phi_j)}$, the correction $(\phi_j - \phi)$ becomes a function of the uncorrected position ϕ_j and not the ideal position ϕ, as desired. If only one dominant term, $-V\sin(-2\pi(\phi_j - \theta))$, is differentiated, and all harmonics higher than two are ignored, the correction simplifies to $(\phi_j - \phi) = -V\sin(-2\pi(\phi_j - \theta))$. This is the correction factor used in this study. Parameters V and θ, measured from the previous 1 ms of position data, are used to correct every current raw position ϕ_j in a few nanoseconds. The correction has only one sine term with spatial period of $\lambda/2$. Its argument, however, is perturbed by periodic error in such a way that it almost exactly compensates for the SSB perturbation of the first-order periodic error.

4. Experimental setup description

A photograph of the setup is provided in Fig. 2. The orthogonal, linearly polarized beams with a split frequency of approximately 3.65 MHz generated within the helium–neon laser first pass through a half wave plate. Rotation of the half wave plate enables variation in the apparent angular alignment (about the beam axis) between the polarization axes and polarizing beam splitter; deviations in this alignment lead to frequency mixing in the interferometer. The light is then incident on a non-polarizing beam splitter (80% transmission) that directs a portion of the beam to a fiber optic pickup after passing

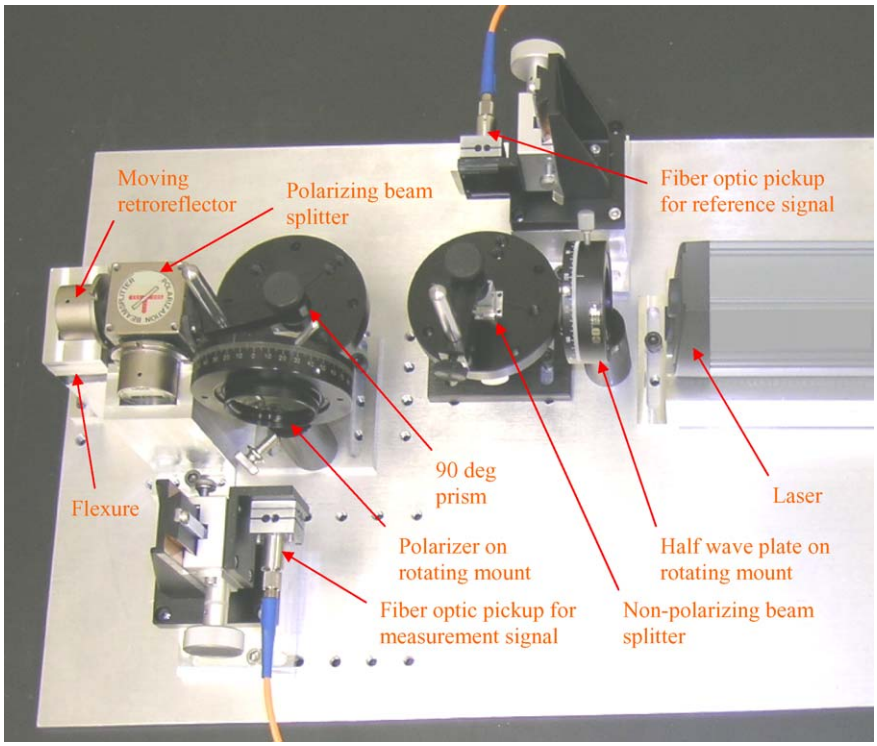

Fig. 2. Photograph of bench-top setup for single-pass heterodyne, Michelson-type interferometer. Frequency mixing is varied by rotation of the half wave plate and/or measurement signal polarizer.

through a fixed angle sheet polarizer (oriented at nominally 45° to the laser orthogonal polarizations). The pickup is mounted on a two rotational degree-of-freedom flexure, which enables efficient coupling of the light into the multi-mode fiber optic. This signal is used as the phase reference in the measurement electronics.

The remainder of the light continues to the polarizing beam splitter where it is nominally separated into its two frequency components that travel separately to the moving and fixed retroreflectors. In this design, motion of the moving retroreflector is achieved using a parallelogram, leaf-type flexure. This enables nominally linear, oscillating displacement at a single frequency. The harmonic motion profile: (1) includes constantly varying velocity, acceleration, and jerk levels that are conveniently adjusted by varying the displacement amplitude; (2) provides a rigorous test of the digital periodic error correction algorithm which assumes negligible jerk. After the beams are recombined in the polarizing beam splitter, they are directed by a 90° prism through a polarizer. Rotation of the polarizer changes the relative amplitude of the intended and mixing-induced interference signals and, therefore, the periodic error. Finally, the light is launched into a fiber optic pickup. This serves as the measurement signal in the measurement electronics.

As noted, the intent of the setup design was to minimize other well-known error contributors [19,20,34] and enable variation in the periodic error nature (i.e., first- or second-order) and amplitude. To isolate periodic error, the setup was designed with zero Abbe offset (i.e., the measurement axis was collinear with the motion axis) and zero dead path difference (i.e., the distance between the polarization beam splitter and the moving retroreflector was equal to the distance between the polarization beam splitter and the fixed retroreflector at initialization). The measurement time (100 ms) and motion amplitude (<200 μm) were kept small to minimize the contribution of air refractive index variations due to the environmental changes. Additionally, the small target motion amplitude resulted in small beam shear (using the flexure dimensions and material properties, the maximum parasitic displacement perpendicular to the beam axis was calculated to be 0.1 for a 100 μm motion amplitude) and angular error (3×10^{-3} μrad for a 100 μm motion amplitude) [35].

Error contributors which were not well-controlled by this setup include cosine error, or an angular misalignment between the measurement and motion axes, due to the small displacement range and mechanical noise (the flexure's low stiffness and light damping caused table vibrations to be transmitted to the moving retroreflector, although these were reduced somewhat by mounting the entire assembly on a rubber mat). However, this study is unique in that the error correction was applied digitally. The analog measurement signal was sampled (0.3 nm resolution) and then the first-order periodic error correction was applied to the digitized data. Because our intent was to compare the (digitized) corrected and uncorrected signals, the cosine and mechanical noise errors can be considered common mode and have little influence on the final results presented here.

5. Experimental results

In this section, we describe the analysis procedure used to extract periodic error from the moving retroreflector dis-

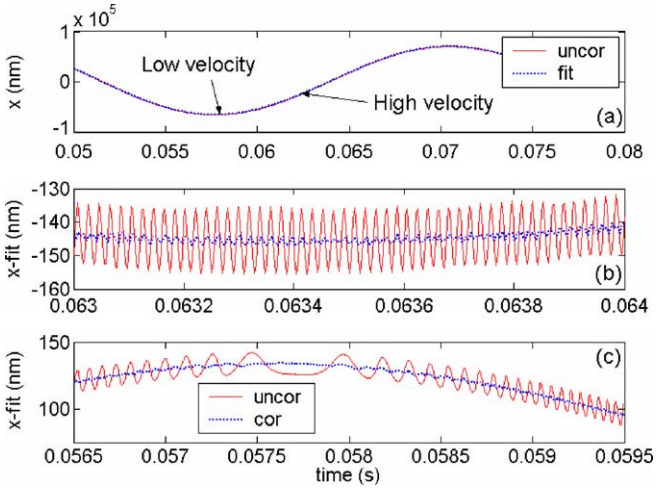

Fig. 3. Example results from data analysis: (a) uncorrected gross flexure motion with sinusoidal non-linear least squares fit superimposed; (b) difference between motion and fit in high velocity region; (c) difference in low velocity region.

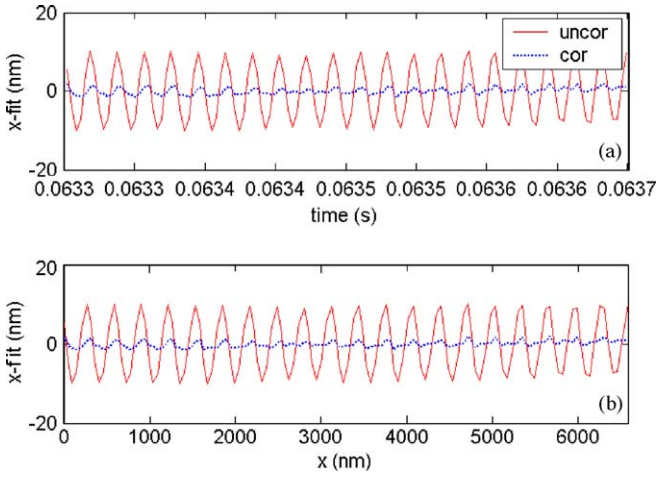

Fig. 4. First-order periodic error reduction example: (a) error vs. time for uncorrected (solid line) and corrected (dotted line) signals; (b) error displacement vs. uncorrected displacement.

placement and present results for various angular orientations of the half wave plate and polarizer. Data was collected by first initiating flexure motion using a light impact (applied by a rubber-tipped mallet) and then recording displacement during the resulting harmonic motion (312.5 kHz sampling frequency).

5.1. Data analysis method

For a unidirectional, constant velocity motion, periodic error can be identified in an interferometer signal by subtracting the least squares straight line fit from the data. In this case, the gross flexure motion is best represented by an exponentially decaying sine wave with some initial phase and, potentially, a dc offset depending on the initial displacement value of the interferometer. To remove the gross motion and isolate the periodic error, a non-linear least squares fit to the data was performed using a function of the form $x(t) = \delta + A\,e^{-\zeta\omega_n t}\sin(\omega_d t + \alpha)$, where δ is the dc offset, A the amplitude, ζ the viscous damping ratio, ω_n is the undamped natural frequency, $\omega_d = \omega_n\sqrt{1-\zeta^2}$ is the damped natural frequency, and α is the initial phase. Once the fit parameters were determined, this function was subtracted from the uncorrected and corrected (first-order error removed) signals and the periodic error levels compared. Typical values for ω_n and ζ were 248.6 rad/s (39.6 Hz) and 0.009 (0.9% damping), respectively.

Example results for the fitting procedure are provided in Fig. 3. A portion of the gross uncorrected motion (solid line) and non-linear least squares fit (dotted line) are shown in panel (a). These signals are then differenced to isolate the periodic error. Panel (b) shows the result for a high velocity section of the original signal, while panel (c) shows the result for a low velocity portion. In both cases, the dominant first-order error (the amplitude was set by angular misalignment of the polarizer) is effectively removed by the correction algorithm. It may also be noted that the least squares fit does not exactly capture the actual motion due to the small curvature and dc offset observed in both panels (b) and (c); however, the low spatial frequency and dc offset errors do not significantly affect the subsequent frequency domain analysis of the periodic error amplitudes before and after correction.

A subset of the high velocity data shown in Fig. 3b is reproduced in Fig. 4a (the dc offset has been removed) and replotted versus uncorrected position in Fig. 4b). For the single pass helium–neon interferometer setup used here, first-order error repeats every 633/2 = 316.5 nm, while second-order completes a full cycle in 633/4 = 158.3 nm. It is now clearly observed that the signal is dominated by first-order error in this case. To identify the first- and second-order error amplitudes, the Fast Fourier transform of the error (versus displacement) was computed and the spatial frequency axis normalized to periodic error order; see Fig. 5. It is shown that the first-order error magnitude has been reduced from 8.4 to 0.9 nm.

A second example is shown in Fig. 6. In this case, both first- and second-order periodic error are present (due to angular misalignments of both the polarizer and half wave plate). The

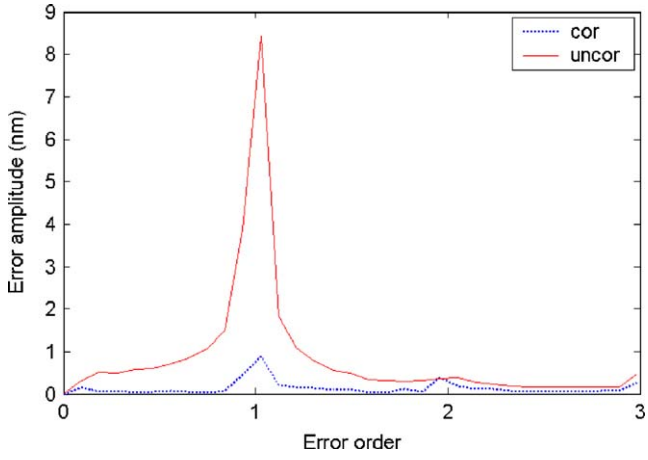

Fig. 5. Fast Fourier transform of error vs. displacement data for corrected (dotted line) and uncorrected (solid line) signals. The first-order error is reduced from 8.4 to 0.9 nm.

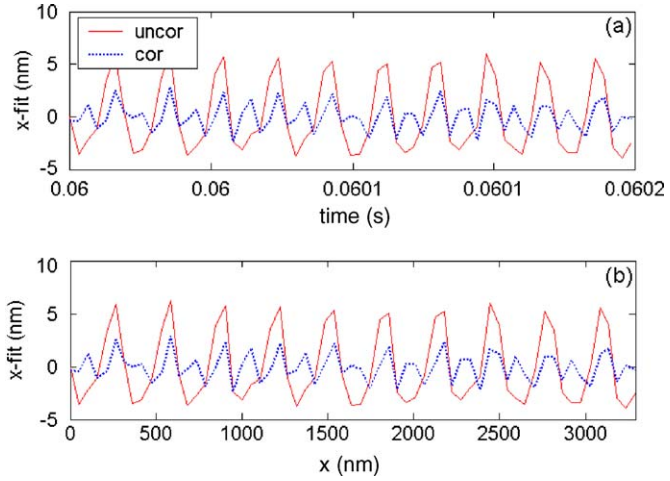

Fig. 6. First- and second-order periodic error example: (a) error vs. time for uncorrected (solid line) and corrected (dotted line) signals; (b) error displacement vs. uncorrected displacement.

spectrum in Fig. 7 shows that the first-order error is reduced from 3.5 to 0.4 nm, while the second-order error remains unaffected (the algorithm does not currently correct this error).

5.2. Error variation with interferometer setup

To explore the independent influences of the half wave plate and polarizer orientations, tests were carried out where one orientation was fixed and the other varied about a nominal value. To represent the results, the uncorrected and corrected first- and second-order periodic error amplitudes (using the Fourier transform data representations shown in Figs. 5 and 7) were extracted for each orientation. Fig. 8 shows the results for a fixed (nominally 45°) polarizer angle and an ±11° variation in the half wave plate angle. While the trend in both error orders is increased amplitude with larger departure from the nominal orientation, the second-order error is more strongly affected. Fig. 9 displays the first-order results only; it is seen that the error amplitude is attenuated in most cases.

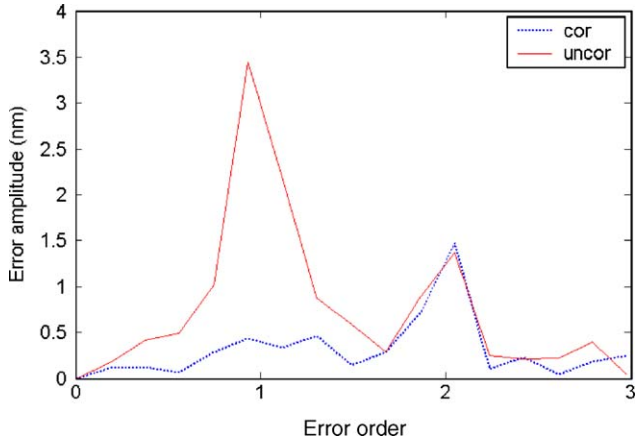

Fig. 7. Fast Fourier transform for example with first- and second-order error. The first-order error is reduced from 3.5 to 0.4 nm.

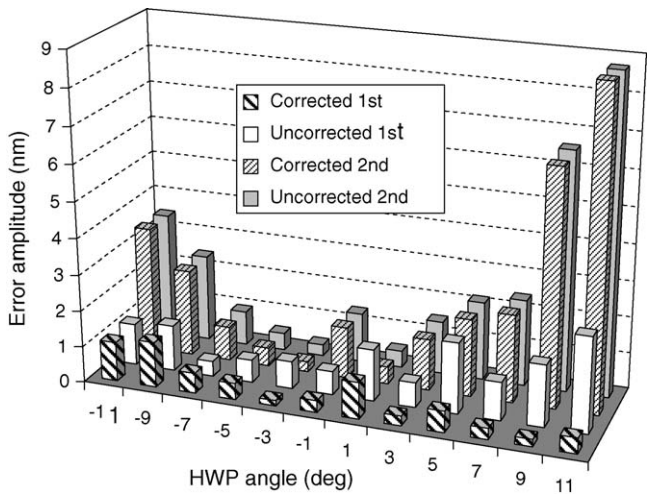

Fig. 8. Variation in first- and second-order periodic error with changes in half wave plate orientation. Results for both the uncorrected and corrected signals are provided.

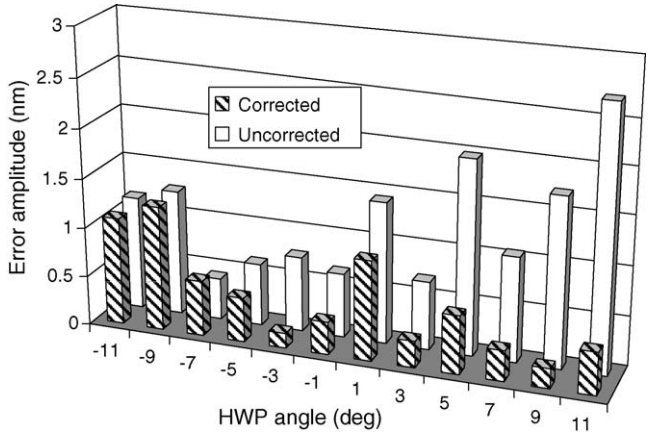

Fig. 9. Variation in first-order periodic error with changes in half wave plate orientation. Results for both the uncorrected and corrected signals are provided.

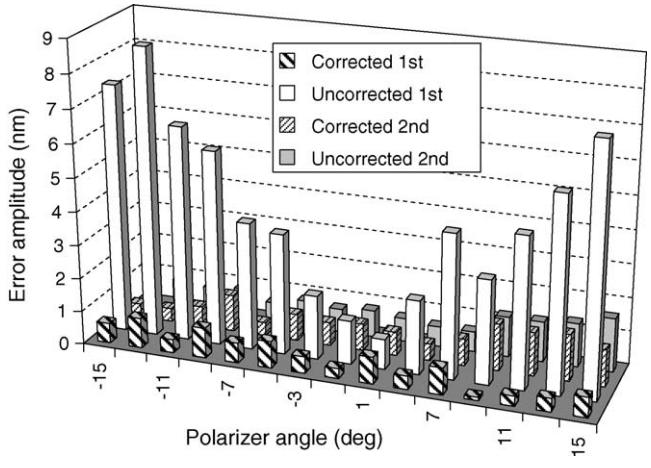

Fig. 10. Variation in first- and second-order periodic error with changes in polarizer orientation. Results for both the uncorrected and corrected signals are provided.

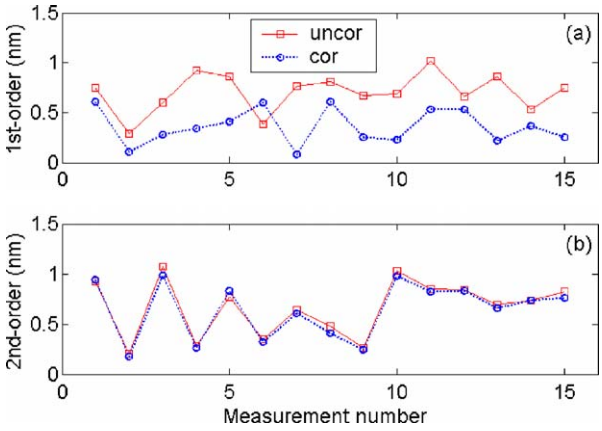

Fig. 11. Repeatability testing results for nominal orientations of half wave plate and polarizer: (a) first-order error amplitudes; (b) second-order error amplitudes.

Fig. 10 displays the results for a variable polarizer angle with a fixed half wave plate angle (the fast axis was nominally aligned with one of the linear polarization directions). In this case, the first-order error is more strongly influenced. In all instances, the correction scheme reduces the first-order periodic error to sub-nm levels. As before, the second-order amplitudes are not affected.

5.3. Repeatability

The final measurement activity was to evaluate the repeatability of the periodic error amplitudes from test to test. To complete this task, displacement was recorded for 15 separate impacts of the flexure-mounted moving retroreflector. Half wave plate and polarizer angles were selected to minimize periodic error using the results provided in Figs. 8–10. The analysis described in Section 5.1 was then completed for each data record and the first- and second-order periodic error amplitudes determined for both the uncorrected and corrected cases. The results are shown in Fig. 11. The standard deviations for the error amplitudes were less than 0.2 nm (first-order) and 0.3 nm (second-order) for the 15 data sets. This compares favorably with the 0.3 nm displacement resolution for the interferometer used in this study.

6. Conclusions

Experimental validation of the digital first-order periodic error reduction scheme described by Chu and Ray [1] was completed using a bench-top setup of a single-pass, heterodyne Michelson interferometer. The strategy was to minimize common error contributors such as Abbe, dead path and environmental errors through the setup design in order to isolate periodic error. Linear, oscillating motion generation was accomplished using a parallelogram, leaf-type flexure. The setup also enabled variation of the periodic error through independent rotation of a half wave plate and polarizer. Experimental results demonstrated that the correction algorithm could successfully attenuate first-order error to sub-nm levels for a wide range of frequency mixing conditions. Additionally, as described in prior publications (e.g., [8,16]), it was found that rotation of the laser beam polarization axes (using the half wave plate) led to increased second-order periodic error, while rotation of the measurement signal polarizer yielded significant first-order error.

Acknowledgement

This work was funded by a grant from Agilent Technologies Inc.

References

[1] Chu D, Ray A. Nonlinearity measurement and correction of metrology data from an interferometer system. In: Proceedings of fourth euspen international conference. 2004. p. 300–1.
[2] Fedotova G. Analysis of the measurement error of the parameters of mechanical vibrations. Meas Tech 1980;23(7):577–80.
[3] Quenelle R. Nonlinearity in interferometric measurements. Hewlett-Packard J 1983;34(4):10.
[4] Sutton C. Nonlinearity in length measurements using heterodyne laser Michelson interferometry. J Phys E: Sci Instrum 1987;20:1290–2.
[5] Barash V, Fedotova G. Heterodyne interferometer to measure vibration parameters. Meas Tech 1984;27(7):50–1.
[6] Bobroff N. Residual errors in laser interferometry from air turbulence and nonlinearity. Appl Opt 1987;26(13):2676–82.
[7] Rosenbluth A, Bobroff N. Optical sources of nonlinearity in heterodyne interferometers. Precision Eng 1990;12(1):7–11.
[8] Stone J, Howard L. A simple technique for observing periodic nonlinearities in Michelson interferometers. Precision Eng 1998;22(4):220–32.
[9] Patterson S, Beckwith J. Reduction of systematic errors in heterodyne interferometric displacement measurement. In: Proceedings of the eighth international precision engineering seminar (IPES). 1995. p. 101–4.
[10] Badami V, Patterson S. A frequency domain method for the measurement of nonlinearity in heterodyne interferometry. Precision Eng 2000;24(1):41–9.
[11] Badami V, Patterson S. Investigation of nonlinearity in high-accuracy heterodyne laser interferometry. In: Proceedings of the 12th annual American society for precision engineering (ASPE) conference. 1997. p. 153–6.
[12] Wu C, Deslattes R. Analytical modeling of the periodic nonlinearity in heterodyne interferometry. Appl Opt 1998;37(28):6696–700.
[13] Wu C, Su C. Nonlinearity in measurements of length by optical interferometry. Meas Sci Technol 1996;7:62–8.
[14] Hou W, Wilkening G. Investigation and compensation of the nonlinearity of heterodyne interferometers. Precision Eng 1992;14(2):91–8.
[15] Hou W, Zhao X. Drift of nonlinearity in the heterodyne interferometer. Precision Eng 1994;16(1):25–35.
[16] Cosijns S, Haitjema H, Schellekens P. Modeling and verifying nonlinearities in heterodyne displacement interferometry. Precision Eng 2002;26:448–55.
[17] Howard L, Stone J. Computer modeling of heterodyne interferometer errors. Precision Eng 1995;12(1):143–6.
[18] Tanaka M, Yamagami T, Nakayama K. Linear interpolation of periodic error in a heterodyne laser interferometer at subnanometer levels. IEEE Trans Instrum Meas 1989;38(2):552–4.
[19] Bobroff N. Recent advances in displacement measuring interferometry. Meas Sci Technol 1993;4:907–26.
[20] Steinmetz C. Sub-micron position measurement and control on precision machine tools with laser interferometry. Precision Eng 1990;12(1):12–24.
[21] Cretin B, Xie W, Wang S, Hauden D. Heterodyne interferometers: Practical limitations and improvements. Opt Commun 1988;65(3):157–62.

[22] Petru F, Cip O. Problems regarding linearity of data of a laser interferometer with a single-frequency laser. Precision Eng 1999;23(1):39–50.
[23] Augustyn W, Davis P. An analysis of polarization mixing errors in distance measuring interferometers. J Vacuum Sci Technol B 1990;8(6):2032–6.
[24] Xie Y, Yu Y. Zeeman laser interferometer errors for high precision measurements. Appl Opt 1992;31(7):881–4.
[25] De Freitas J, Player M. Importance of rotational beam alignment in the generation of second harmonic errors in laser heterodyne interferometry. Meas Sci Technol 1993;4:1173–6.
[26] De Freitas J, Player M. Polarization effects in heterodyne interferometry. J Mod Opt 1995;42(9):1875–99.
[27] De Freitas J. Analysis of laser source birefringence and dichroism on nonlinearity in heterodyne interferometry. Meas Sci Technol 1997;8:1356–9.
[28] Li B, Liang J. Effects of polarization mixing on the dual-wavelength heterodyne interferometer. Appl Opt 1997;36(16):3668–72.
[29] Park B, Eom T, Chung M. Polarization properties of cube-corner retroreflectors and their effects on signal strength and nonlinearity in heterodyne interferometers. Appl Opt 1996;35(22):4372–80.
[30] Wu C, Lawall J, Deslattes R. Heterodyne interferometer with subatomic periodic nonlinearity. Appl Opt 1999;38(19):4089–94.
[31] Oldham N, Kramar J, Hetrick P, Teague E. Electronic limitations in phase meters for heterodyne interferometry. Precision Eng 1993;15(3):173–9.
[32] Schmitz T, Beckwith J. Acousto-optic displacement-measuring interferometer: A new heterodyne interferometer with Angstrom-level periodic error. J Mod Opt 2002;49(13):2105–14.
[33] Schmitz T, Beckwith J. An investigation of two unexplored periodic error sources in differential-path interferometry. Precision Eng 2002;27(3):311–22.
[34] Schmitz T, Evans C, Davies A, Estler WT. Displacement uncertainty in interferometric radius measurements. Ann CIRP 2002;51(1):451–4.
[35] Smith ST. Flexures: elements of elastic mechanisms. Amsterdam: Gordon and Breach Science Publishers; 2000.